PHYSICAL REVIEW B **111**, 085432 (2025)

Multifield tunable valley splitting and anomalous valley Hall effect in two-dimensional antiferromagnetic MnBr

Yiding Wang,[1,2,3,*] Hanbo Sun,[3,*] Chao Wu,[3] Weixi Zhang,[2,†] San-Dong Guo,[4] Yanchao She,[1,2,‡] and Ping Li[3,5,6,§]
[1]*School of Physics and Mechatronics Engineering, Jishou University, Jishou, Hunan 416000, People's Republic of China*
[2]*Department of Physics and Electronic Engineering, Tongren University, Tongren 554300, People's Republic of China*
[3]*State Key Laboratory for Mechanical Behavior of Materials, School of Materials Science and Engineering, Xi'an Jiaotong University, Xi'an, Shaanxi 710049, People's Republic of China*
[4]*School of Electronic Engineering, Xi'an University of Posts and Telecommunications, Xi'an 71021, People's Republic of China*
[5]*State Key Laboratory of Silicon and Advanced Semiconductor Materials, Zhejiang University, Hangzhou 310027, People's Republic of China*
[6]*State Key Laboratory for Surface Physics and Department of Physics, Fudan University, Shanghai 200433, People's Republic of China*

(Received 21 November 2024; revised 17 January 2025; accepted 18 February 2025; published 28 February 2025)

Compared to the ferromagnetic materials that realize the anomalous valley Hall effect by breaking time-reversal symmetry and spin-orbit coupling, the antiferromagnetic materials with joint spatial inversion and time-reversal (PT) symmetry are rarely reported to achieve the anomalous valley Hall effect. Here, we predict that the antiferromagnetic monolayer MnBr possesses spontaneous valley polarization. The valley splitting of the valence band maximum is 21.55 meV at K and K' points, which originates from Mn-$d_{x^2-y^2}$ orbital by analyzing the effective Hamiltonian. Importantly, monolayer MnBr has zero Berry curvature in the entire momentum space but nonzero spin-layer locked Berry curvature, which offers the condition for the anomalous valley Hall effect. In addition, the magnitude of valley splitting can be signally tuned by the strain, magnetization rotation, electric field, and built-in electric field. The electric field and built-in electric field induce spin splitting due to breaking the P symmetry. Therefore, the spin-layer locked anomalous valley Hall effect can be observed in MnBr. More remarkably, the ferroelectric substrate Sc_2CO_2 can tune monolayer MnBr to realize the transition from metal to valley polarization semiconductor. Our findings not only extend the implementation of the anomalous valley Hall effect, but also provide a platform for designing low-power and nonvolatile valleytronics devices.

DOI: 10.1103/PhysRevB.111.085432

I. INTRODUCTION

Valley degree of freedom is the third degree of freedom for electrons outside of charge and spin, and has recently attracted extensive attention since it provides remarkable opportunities for realizing the next-generation of ultrafast, ultrahigh capacity, low power consumption, and nonvolatile devices [1–8]. The valley refers to a local energy maximum or minimum point in the valence or conduction band; this energy extremum is robust against impurity scattering and phonon due to the large separation in the momentum space [9]. The current focus of valley investigation is understanding how to stably manipulate the valley degrees of freedom, thereby generating robust valley polarization [10–19]. Physically, there are two strategies to realize valley polarization. One is optical excitation with circularly polarized light [20,21]. When the light is removed, the material retains its original symmetry. The other involves breaking symmetry structurally, which is an irreversible process [22,23]. The former is a dynamic process, while the latter is especially concerned with the intrinsic valley polarization.

There are also two kinds of ways to achieve the intrinsic valley polarization. One is to break the symmetry of spatial inversion (P) via ferroelectric polarization [24,25], and the other breaks the time-reversal symmetry (T) through magnetism [10–19]. This kind of material is named ferrovalley material [10]. To date, achieving the ferrovalley via breaking T symmetry has mainly focused on ferromagnetic (FM) materials. Compared with the FM materials, antiferromagnetic (AFM) material is robust against external magnetic perturbation, has high storage density, and possesses ultrafast writing speed (about three orders of magnitude higher than the FM material) due to the zero magnetic moment [26,27]. It is well known that the two sublattices have opposite spin vectors for the AFM hexagonal lattice. Both the P and T symmetries are broken, but the joint symmetry PT is retained. Therefore, the AFM ferrovalley provides an inviting potential for spintronic and valleytronic applications. Unfortunately, the spontaneous valley polarization in AFM materials is exceedingly rare, which makes the circumstances worse. Simultaneously, the anomalous valley Hall effect is undesirably suppressed for the AFM materials.

In this work, based on the density functional theory (DFT) and Hamiltonian model, we propose that the AFM monolayer MnBr is a highly fascinating candidate for abundant valley contrasting physics. Our results show that monolayer MnBr is a semiconductor with spin-up and spin-down band degeneracy without the spin-orbit coupling (SOC) effect. When

---

[*] These authors contributed equally to this work.
[†] Contact author: zhangwwxx@sina.com
[‡] Contact author: ycshe@xtu.edu.cn
[§] Contact author: pli@xjtu.edu.cn

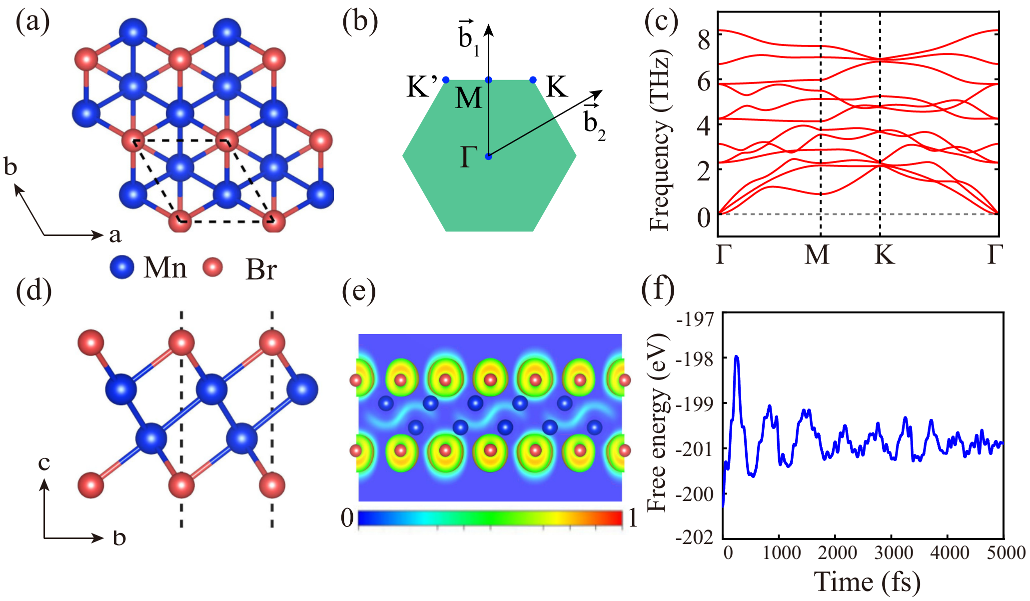

FIG. 1. (a),(d) The top and side views of the crystal structure for monolayer MnBr, respectively. The blue and pink balls represent Mn and Br elements, respectively. (b) The Brillouin zone (BZ) of the honeycomb lattice with the reciprocal lattice vectors $\vec{b}_1$ and $\vec{b}_2$. The Γ, K, K', and M are high-symmetry points in the BZ. (c) The calculated phonon dispersion curves along the high-symmetry lines with the first BZ of MnBr. (e) Electron localization function of monolayer MnBr. (f) Total energy fluctuations of monolayer MnBr during 5 ps AIMD simulation at 300 K.

the SOC is included, the valence band maximum (VBM) has 21.55 meV valley splitting at K and K' points, which originates from the Mn-$d_{x^2-y^2}$ orbital by analyzing the effective Hamiltonian. Importantly, not only can the value of valley splitting be tuned by the strain, magnetization rotation, electric field, and built-in electric field, but also the phase transition of valley polarized semiconductor to metal can be controlled by ferroelectric substrate Sc_2CO_2. Our findings open an avenue for the investigation of the valley physical quantity in the AFM material, realizing energy conserving, fast operating spintronic and valleytronic devices.

II. COMPUTATIONAL METHODS

Based on the framework of the DFT, we investigate the electronic and magnetic properties using the Vienna *ab initio* simulation package (VASP) [28,29]. The generalized gradient approximation (GGA) with the Perdew-Burke-Ernzerhof (PBE) functional is employed to describe the exchange-correlation energy [30]. The plane-wave basis with a kinetic energy cutoff of 500 eV is used. A vacuum of 30 Å is added along the c axis, to avoid the interaction between the sheet and its periodic images. The convergence criteria of the force and the total energy are set to -0.005 eV/Å and 10^{-6} eV, respectively. To describe strongly correlated $3d$ electrons of Mn, the GGA. $+\,U$ method is adopted with the effective U value ($U_{\text{eff}} = U - J$) of 4 eV [31–33]. The zero damping DFT-D3 method of Grimme is considered for the van der Waals (vdW) correction in $MnBr/Sc_2CO_2$ heterostructure [34]. To explore the dynamical stability, the phonon spectra are calculated by the PHONOPY code using a finite displacement approach with a $4 \times 4 \times 1$ supercell [35]. Thermal stability is evaluated using *ab initio* molecular dynamics (AIMD) with a $3 \times 3 \times 1$ supercell [36]. Moreover, to investigate the Berry curvature, the maximally localized Wannier functions (MLWFs) are used to construct an effective tight-binding Hamiltonian by WANNIER90 code [37,38].

III. RESULTS AND DISCUSSION

A. Structure and stability

Figures 1(a) and 1(d) exhibit the crystal structure of monolayer MnBr. The monolayer MnBr possesses a two-dimensional (2D) hexagonal lattice and consists of septuple layers of Br-Mn-Mn-Br. There are three Br and three Mn atoms nearest to each Mn atom, forming an octahedral crystal field. The space group of monolayer MnBr is $P\bar{3}m1$. The lattice constant of MnBr is optimized to 3.60 Å. To evaluate the dynamic stability, the phonon spectra are investigated. As shown in Fig. 1(c), the absence of imaginary frequencies verifies that monolayer MnBr is dynamically stable. To explore the bonding features of monolayer MnBr, we calculated its electron localization function (ELF). As shown in Fig. 1(e), the electrons are mainly localized between Mn and Mn atoms and around the Br atoms, showing typical covalent bonding for the Mn-Mn bond and ionic bonding for the Mn-Br bond. Moreover, the thermodynamic stability is also estimated by the AIMD calculation. As shown in Fig. 1(f), the total energies of monolayer MnBr fluctuate very little when evolving during 5 ps at 300 K, indicating that monolayer MnBr has good thermal stability.

B. Magnetic property

The valence electronic configuration of an isolated Mn atom is $3d^5 4s^2$. For the MnBr crystal, the Mn atom would

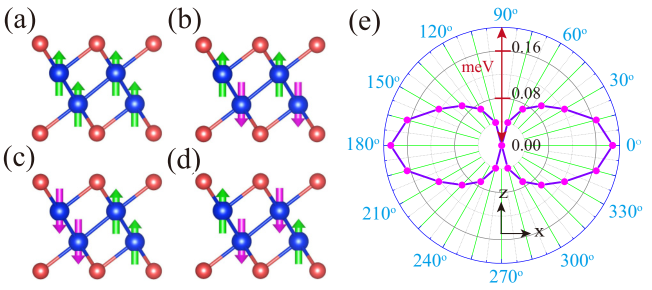

FIG. 2. (a)–(d) FM, AFM1, AFM2, and AFM3 configurations for monolayer MnBr, respectively. (e) Angular dependence of the MAE of monolayer MnBr with the direction of magnetization lying on the *xz* plane.

lose three electrons to the three neighboring Br atoms due to its surroundings, resulting in the electronic configuration of $3d^4 4s^0$. In the octahedral crystal field, the d orbital is split into two groups: t_{2g} (d_{xy}, d_{yz}, d_{xz} orbitals) and e_g ($d_{x^2-y^2}$, d_{z^2} orbitals). According to the Pauli exclusion principle and Hund's rule, the electronic configuration of Mn would half fill the t_{2g} orbitals and half fill one of two e_g orbitals. Therefore, the magnetic moment of each Mn atom is $4\mu_B$.

To confirm the magnetic ground state of monolayer MnBr, as shown in Figs. 2(a)–2(d), four possible magnetic configurations, FM, AFM1, AFM2, and AFM3, are considered. We calculate the total energy difference between FM, AFM1, AFM2, and AFM3 using the GGA. + U method. According to previous reports [30–32], for the selection of the U value for the Mn atom in 2D materials, we choose $U_{\text{eff}} = 4$ eV to investigate monolayer MnBr. The AFM1 state is 4.414 eV, 3.305 eV, and 2.235 eV lower in energy than the FM, AFM2, and AFM3 states, respectively.

For 2D magnetic materials, the out-of-plane direction is the direction of easy magnetization that is the basis for all research. Therefore, we investigate the magnetic anisotropy energy (MAE), which is defined as MAE $= E_{100} - E_{001}$, where E_{100} and E_{001} denote the total energies of the magnetic moment along [100] and [001] directions, respectively. The MAE is 0.18 meV, showing magnetization along the [001] direction. In addition, for the octahedral crystal field of monolayer MnBr, the angular dependence of the MAE can be written employing the equation

$$\text{MAE} = K_1 \cos^2\theta + K_2 \cos^4\theta, \tag{1}$$

where θ is the azimuthal angle of rotation and K_1 and K_2 are the anisotropy constants. If $K_1 < 0$, the benefited magnetization direction will be along the out-of-plane direction (z axis), while $K_1 > 0$ indicates that it will be parallel to the plane (x axis). The MAE of monolayer MnBr exhibits a good fit of Eq. (3), as shown in Fig. 2(e); it indicates that the MAE strongly depends on the direction of magnetization in the xz plane.

C. Band structure and anomalous valley Hall effect

Next, we concentrate on band structure and associated valley splitting of monolayer MnBr. When the SOC is switched off, as shown in Fig. 3(a), the spin-up and spin-down bands are degenerate. Moreover, it is an indirect band gap semiconductor with a 1.89 eV band gap. The band gap using the HSE06 functional is 2.67 eV, as shown in Fig. S1 of the Supplemental Material [39]. The VBM appears at the K/K' points and they are degenerate, while the conduction band minimum (CBM) exhibits an M point. Figures 3(b) and 3(c) show the orbital-resolved band structure; we find that the VBM bands are dominated by Mn $d_{x^2-y^2} + d_{z^2}$ orbitals, while the CBM bands are mainly contributed by Mn $d_{xy} + d_{yz} + d_{xz}$ orbitals. In the existence of SOC, as shown in Fig. 3(d), the valley degeneracy of K and K' at the VBM bands disappears. Simultaneously, the valley polarization is spontaneously induced, and the valley splitting is 21.55 meV. The orbital-resolved band structures, as shown in Figs. 3(e) and 3(f), are completely consistent with and without the SOC effect. Moreover, we calculate the projected density of states (PDOS) of monolayer MnBr, as shown in Fig. S2 [39]. It is clearly observed that the d orbitals of Mn and the p orbitals of Br have very strong hybridization.

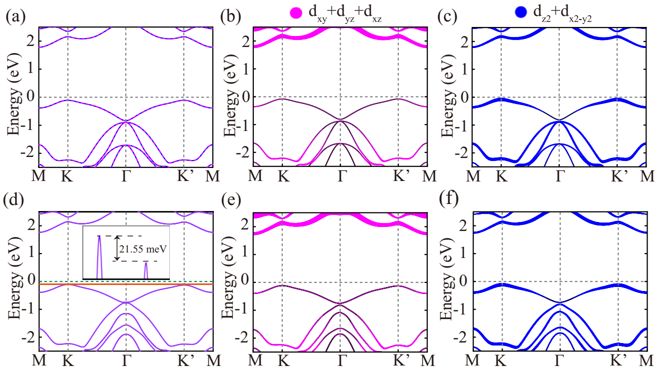

FIG. 3. Band structures of monolayer MnBr (a) without and (d) with the SOC effect. Band structures of monolayer MnBr without the SOC effect are projected on the (b) $d_{xy} + d_{yz} + d_{xz}$ and (c) $d_{x^2-y^2} + d_{z^2}$ orbitals, and those with the SOC effect are projected on the (e) $d_{xy} + d_{yz} + d_{xz}$ and (f) $d_{x^2-y^2} + d_{z^2}$ orbitals. The magenta dotted line and blue line show spin-down and spin-up bands, respectively. The valence band valley splitting is shown by the orange shading.

To understand the underlying mechanism for the ferrovalley effect in monolayer MnBr, we adopted $|\psi_v^\tau\rangle = |d_{x2-y2}\rangle) \otimes |\uparrow\rangle$ to construct an effective Hamiltonian. It is well known that the orbital angular momentum of the d_{z^2} orbital is zero. Thus, we do not consider the d_{z^2} orbital, since the d_{z^2} orbital does not cause valley splitting. Based on the SOC effect as a perturbation term, the effective Hamiltonian can be written as

$$\hat{H}_{\text{SOC}} = \lambda \hat{S} \cdot \hat{L} = \hat{H}^0_{\text{SOC}} + \hat{H}^1_{\text{SOC}}, \tag{2}$$

where $\hat{S}$ and $\hat{L}$ are spin angular and orbital angular operators, respectively. $\hat{H}^0_{\text{SOC}}$ and $\hat{\text{H}}^1_{\text{SOC}}$ stand for the interactions between the same spin states and between opposite spin states, respectively. Here, we only consider the spin-up band. Therefore, the $\hat{H}^1_{\text{SOC}}$ term can be ignored. Consequently, $\hat{H}^0_{\text{SOC}}$ can be written using polar angles,

$$\hat{H}^0_{\text{SOC}} = \lambda \hat{S}_{z'}(\hat{L}_z \cos\theta + \tfrac{1}{2}\hat{L}_+ e^{-i\phi} \sin\theta + \tfrac{1}{2}\hat{L}_- e^{+i\phi} \sin\theta). \tag{3}$$

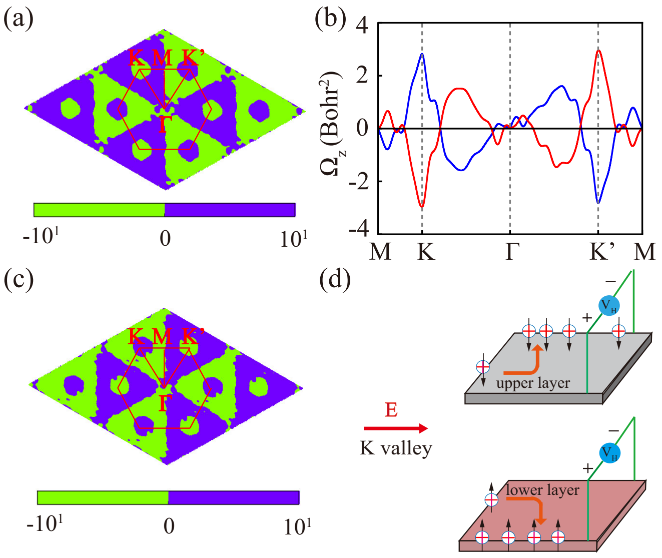

FIG. 4. The Berry curvatures of monolayer MnBr for (a) spin up and (c) spin down in the entire BZ region. (b) The Berry curvature along the high symmetry line. The red and blue lines show spin-up and spin-down Berry curvatures, respectively. (d) Schematic diagram of valley layer spin Hall effect. The holes are represented by the + symbol. Upward and downward arrows denote the spin-up and spin-down carriers, respectively.

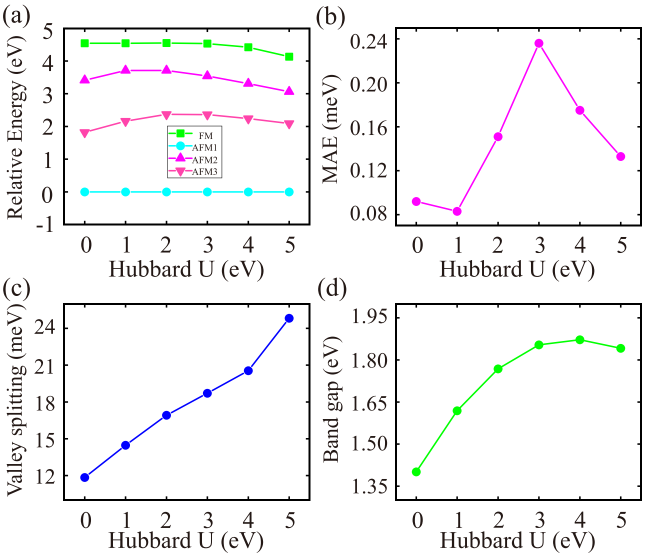

FIG. 5. (a) The total energies of monolayer MnBr for different magnetic configurations with the different Hubbard U values, which are defined relative to that of the AFM1 state. (b) The MAE with the different Hubbard U values. (c) The valley splitting with the different Hubbard U values. (d) The global band gap with the different Hubbard U values.

In the out-of-plane magnetization situation, $\theta = \phi = 0^\circ$; then the $\hat{H}^0_{\mathrm{SOC}}$ term can be simplified as

$$\hat{H}^0_{\mathrm{SOC}} = \lambda \hat{S}_z \hat{L}_z, \tag{4}$$

The λ is the SOC strength of MnBr, which is $\lambda = 23.58$ meV. The energy level of the valley for the VBM can be described by $E_v^\tau = \langle \psi_v^\tau | \hat{H}^0_{\mathrm{SOC}} | \psi_v^\tau \rangle$. Then, the valley splitting can be described by

$$E_v^K - E_v^{K'} = \langle d_{x^2-y^2} | \hat{H}^0_{\mathrm{SOC}} | d_{x^2-y^2} \rangle \approx \beta, \tag{5}$$

where $\beta = \lambda \langle d_{x2-y2} | \hat{S}_{z'} | d_{x2-y2} \rangle$. The analytical model confirms that the valley splitting is consistent with our DFT result ($E_v^K - E_v^{K'} = 21.55$ meV).

To describe the valley contrasting physics in monolayer MnBr, we calculate its Berry curvature. Due to the joint PT symmetry in monolayer MnBr, the Berry curvature is zero in entire the BZ region. However, monolayer MnBr has two layers of Mn atoms. For each layer of Mn atoms, the PT symmetry is broken. Therefore, the AFM1 state generates spin-layer locking, which makes the spin-up and spin-down Berry curvatures have opposite sign and be equal in magnitude. Figures 4(a)–4(c) showthe spin-up and spin-down Berry curvatures in the entire 2D BZ region and along the high-symmetry line. The Berry curvatures at the K and K' points have equal magnitude, while they exhibit opposite signs for the same valley of different spin channels and different valleys of the same spin channel. It indicates production of spin-layer locking Berry curvature and the typical valley feature. As the Fermi level is moved between the K and K' valleys in the VBM band, the spin-up and spin-down holes of the K valley will be produced and accumulate on the opposite boundary of different layers. As shown in Fig. 4(d), we name this phenomenon the valley layer spin Hall effect, but the anomalous valley Hall effect is nonexistent due to spin degeneracy.

We observe the band structure and valley splitting when the strength of on-site correlation Hubbard U is varied. First, we confirm the magnetic ground state of Hubbard U at 0–5 eV. As shown in Fig. 5(a), the AFM1 state is much lower than the other three magnetic configurations, indicating that AFM1 is robust. Besides, we explore the MAE at varied Hubbard U. As shown in Fig. 5(b), the variation range is only 0.08–0.24 meV, showing that the U value has little influence on MAE. Importantly, the directions of easy magnetization are all out of plane at varied Hubbard U. On this basis, we calculate the band structures without and with the SOC (see Fig. S3) [39]. We can clearly observe that the U value has little effect on the band structure. In the absence of SOC, spin-up and spin-down bands are still degenerate. Meanwhile, the VBM and CBM remain at K/K' and M points, respectively. When the SOC is included, the valley split line increases from 11.85 to 24.82 meV. In addition, the band gap is increased from 1.40 to 1.87 eV and then goes down to 1.84 eV. In a word, the band gap change is not obvious.

D. Strain tuned valley splitting

In device manufacturing, 2D materials are usually supported by a substrate, which may introduce strain to the 2D material due to lattice mismatches [40–42]. Therefore, it is very important that the properties of 2D materials remain unchanged under strain. In the following, we are mainly concerned about the effect of strain on valley splitting. In the calculations, the biaxial strain is defined as $\varepsilon = (a - a_0)/a_0 \times 100\%$, where a and a_0 denote the lattice constant after and before in-plane biaxial strain is applied, respectively. We explore the in-plane biaxial strain in the reasonable range of -5%

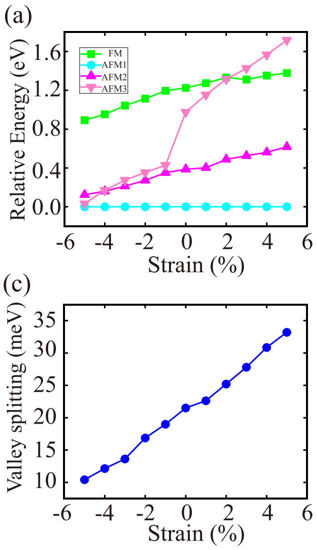

FIG. 6. (a) The total energies of monolayer MnBr for different magnetic configurations as a function of strain, which are defined relative to that of the AFM1 state. (b) The MAE as a function of strain. (c) The valley splitting as a function of strain. (d) The global band gap as a function of strain.

to 5%. As shown in Fig. 6(a), the magnetic ground state is always AFM1 at −5% to 5%. It shows that AFM1 is very stable under strain. Besides, as shown in Fig. 6(b), the MAE increased from 0.08 to 0.24 meV under strain. And all easy magnetization directions are out of plane. The band structures under various strains are shown in Figs. S4 and S5 [39]. As shown in Fig. 6(c), we find that the valley splitting increases from 10.42 meV at −5% strain to 33.21 meV at 5% strain. It means that the strain is significantly adjustable using the valley splitting. In addition, the band gap also increases from 1.69 to 2.01 eV [see Fig. 6(d)]. Interestingly, the variation trend of valley splitting and band gap is consistent with the MAE. This finding means not only that the magnetic ground state of monolayer MnBr has strain resistance, but also that valley splitting can be effectively tuned by strain.

E. Magnetic tuned valley splitting

Monolayer MnBr has both AFM and ferrovalley properties, which is typical of a multiferroic material. We are very curious about the coupling strength between multiferroic orders. Hence, we explore the effect of the magnetization direction on the valley splitting. Figure 7 shows the valley splitting of the valence band as a function of the magnetization direction. When the magnetization direction rotates from in plane (0°) to out of plane (90°), the valley splitting of valence continuously increases from 0.91 to 21.55 meV. If the magnetization direction continues to rotate to the $-x$ axis (180°), the value of valley splitting continuously decreases from the maximum to 0.91 meV. Interestingly, the variation trend of valley splitting is opposite to that of the MAE. Namely, the valley splitting is the smallest when the MAE is maximum, while the valley splitting is the largest when the MAE is minimal. The valley splitting exhibits a twofold relationship, which further confirms that the established effective Hamiltonian of valley splitting is correct.

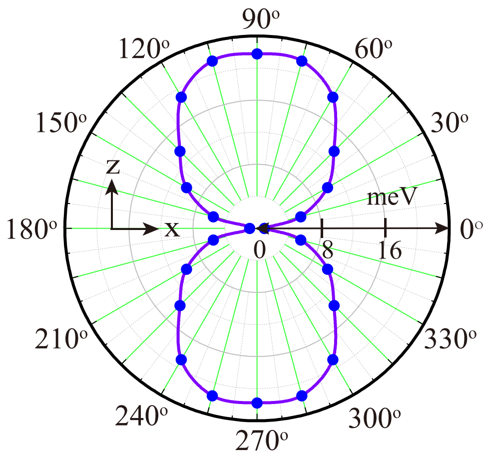

FIG. 7. Angular dependence of the valence band valley splitting of monolayer MnBr with the direction of magnetization lying on the xz plane is shown by the purple line.

F. Electric field tuned valley splitting

From the device application point of view, the electric field is the most effective means of tuning the physical quantity [42,43]. Most importantly, the electric fields enable fast, nondamaging, and efficient regulation of the device. Therefore, we investigate the valley splitting with the electric field 0.0–0.3 V/Å. An out-of-plane electric field breaks the P symmetry. As a result, the PT symmetry of the monolayer MnBr system disappears. Eventually, the spin splitting is caused. Importantly, the magnetic ground state is still in AFM1 configuration, and the direction of easy magnetization is also out of plane. As shown in Fig. 8(a), we can clearly observe that the electric field can effectively tune the value of valley splitting. The valley splitting decreased from 21.55 meV at 0.0 V/Å to 20.70 meV at 0.3 V/Å. Simultaneously, the global band gap decreased from 1.870 to 1.854 eV. Figure 8(c) shows the band structure of the Mn layer resolved with SOC at $E = 0.3$ V/Å. One can clearly observe Mn layer splitting of the band structure under the external electric field. Hence, in the hole-doping case, the spin-up holes of the K valley will be produced and accumulate on one boundary of the lower layer under an in-plane electric field [see Fig. 8(d)]. Consequently, the spin-layer locked anomalous valley Hall effect will be observed. This characteristic indicates that monolayer MnBr is an ideal candidate for high performance valleytronic devices.

Besides, we have calculated the spin splitting of the VBM at the K point in an external electric field, as shown in Fig. S6 [39]. It can be found that spin splitting increases with the increase of external electric field, which means that the anomalous valley Hall effect can be observed over a larger range.

G. Built-in electric field tuned valley splitting

The successful preparation of Janus structure enriches the intrinsic physical properties of 2D materials [44]. Since the

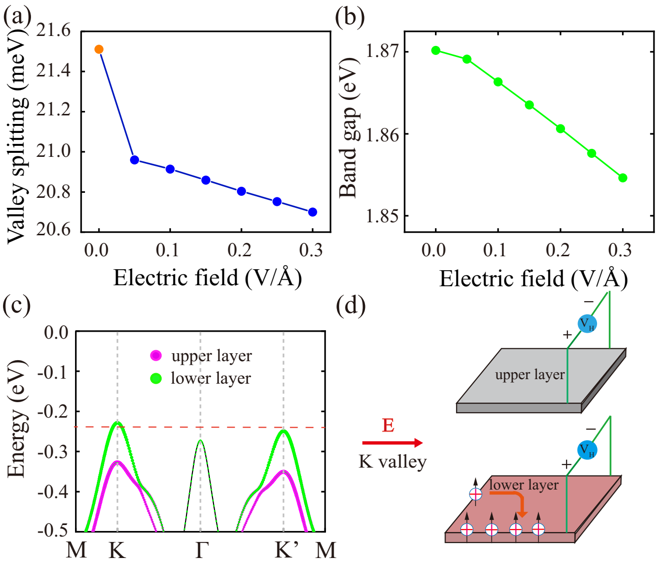

FIG. 8. (a) The valley splitting as a function of electric field for monolayer MnBr. (b) The global band gap as a function of electric field. (c) The band structure of Mn layer resolved with SOC at $E = 0.3$ V/Å. (d) Schematic diagram of spin-layer locked anomalous valley Hall effect in the hole-doped monolayer MnBr at the K and K' valleys. The holes are represented by the + symbol. Downward arrows denote the spindown carriers.

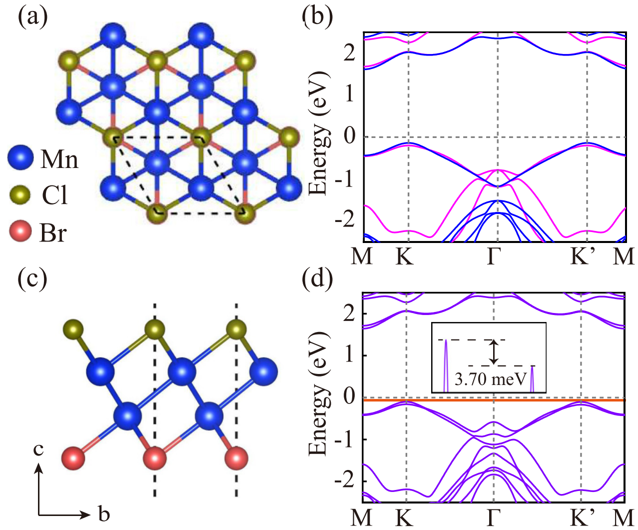

FIG. 9. The (a) top and (c) side views of the crystal structure for monolayer Mn_2ClBr. The blue, brown, and pink balls represent Mn, Cl, and Br elements, respectively. (b) Spin-polarized band structure of monolayer Mn_2ClBr. The blue and magenta lines denote spin-up and spin-down bands, respectively. (d) Band structure with the SOC effect. The valence band valley splitting is shown by the orange shading.

upper and lower surfaces of the Janus structure are not equivalent, a large built-in electric field is generated. Interestingly, our previous investigation found that the built-in electric field can effectively tune the band structure and topological phase transition [15]. By replacing the upper atomic layer of Br with Cl or I, as shown in Figs. 9(a), 9(c) and Figs. S7(a), S7(c) [39], the space group and the point group are reduced from $P\bar{3}m1$ and D_{3d} to $P3m1$ and C_{3v}, respectively. Our calculation results indicate that the energy of the AFM1 state is 4.138 eV (4.804 eV), 3.205 eV (3.585 eV), and 2.146 eV (2.507 eV) lower than the FM, AFM2, and AFM3 states for Mn_2ClBr (Mn_2BrI), respectively.

In order to quantitatively analyze the effect of built-in electric field on valley splitting, we define the built-in electric field as $E_{in} = (\Phi_2 - \Phi_1)/\Delta h$. The Φ_1 and Φ_2 denote the electrostatic potential at the top and bottom of Mn_2ClBr and Mn_2BrI (see Fig. S8) [39], respectively. The Δh is the structural height of Mn_2ClBr and Mn_2BrI. According to the plane averaged electrostatic potential of monolayer Mn_2ClBr and Mn_2BrI along the z axis, the electrical polarization can be clearly observed. Therefore, the built-in electric fields are 0.04 V/Å (Mn_2ClBr), and 0.07 V/Å (Mn_2BrI). In the absence of SOC, the built-in electric field produces the same effect as the electric field, resulting in spin splitting [see Figs. 9(b) and S7(b)]. Unlike the electric field, the built-in electric field raises the energy level of the valence Γ point. The VBM of Mn_2ClBr remains the K/K' point, while the VBM of Mn_2BrI becomes the Γ point. Importantly, the built-in electric field of monolayer Mn_2ClBr reduces the valley splitting to 3.70 meV [see Fig. 9(d)]. It is worth noting that the spin splitting can also be achieved with a built-in electric field. Therefore, the spin-layer locked anomalous valley Hall effect can also be realized. Hence, it is further confirmed that the built-in electric field caused by the quantum confined effect can effectively tune the physical properties.

H. Ferroelectric substrate tuned valley splitting

A ferroelectric substrate is also one of the common means of tuning physical quantities. Therefore, we explore the ferroelectric substrate Sc_2CO_2 tuned valley splitting of monolayer MnBr. We find that the 1 × 1 unit cell of MnBr is matched to the 1 × 1 Sc_2CO_2 with a lattice mismatch rate of less than 5%. Here, we consider three typical configurations, as shown in Figs. 10(a), 10(d) Figs. S9(a), S9(d), and Figs. S10(a), S10(d) [39], i.e., the lower layer Mn atom of MnBr being in hollow, top-Sc, and top-O positions of the Sc_2CO_2, respectively. As listed in Table SI [39], the total energy results indicate that the hollow and top-Sc configurations are the most stable for polarization down and polarization up, respectively. Besides, the easy magnetization direction of all structures is in the out-of-plane direction, as listed in Table SII [39]. As the Sc_2CO_2 is polarized $P\uparrow$, as shown in Figs. 10(b), S9(b), and S10(b) [39], the spin-polarized band structures show metallic properties. In contrast, the band gap of the heterostructure is ~1.40 eV for the polarization $P\downarrow$ of Sc_2CO_2 [see Figs. 10(e), S9(e), and S10(e)] [39]. Importantly, the VBM remains at K/K' point, and the K and K' in energy are degenerate. When the SOC is included, band structures of $P\uparrow$ heterostructure show metallic properties, as shown in Figs. 10(c), S9(c), and S10(c) [39]. Interestingly, when the Sc_2CO_2 polarization switches to $P\downarrow$, the valley degeneracy of K and K' disappears, and they exhibit ~7.00 meV valley splitting [see Figs. 10(f), S9(f), and S10(f)] [39]. It indicates that the transition from metal phase to valley

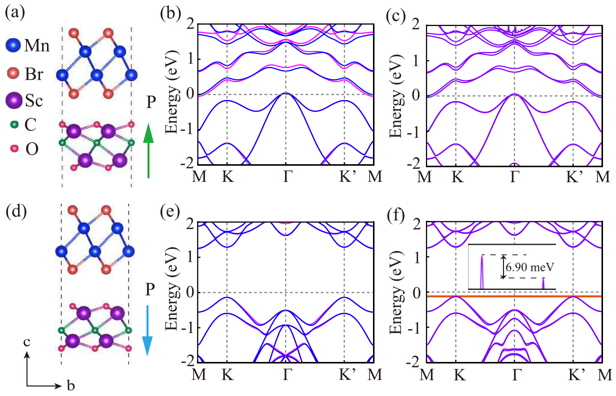

FIG. 10. Side views of (a) $P\uparrow$ state and (d) $P\downarrow$ state $MnBr/Sc_2CO_2$ heterostructures with the hollow configuration. (b),(e) Spin-polarized band structure of $MnBr/Sc_2CO_2$ heterostructures for (b) polarization up and (e) polarization down with the hollow configuration. The blue and magenta lines denote spin-up and spin-down bands, respectively. (c),(f) Band structure with the SOC of $MnBr/Sc_2CO_2$ heterostructures for (c) polarization up and (f) polarization down with the hollow configuration.

polarization semiconductor can be realized when the direction of ferroelectric polarization is switched.

In order to systematically understand the physical mechanism of multifield tunable valley splitting, we calculate the SOC strength of Mn atoms in monolayer MnBr in the multifield. As shown in Fig. S11 [39], when the magnetization direction is along the z axis, the valley splitting increases with the decrease of SOC strength for the onsite correlation, strain, and electric field. More interestingly, when the direction of magnetization changes, the valley splitting increases with the increase of SOC strength. Here, an important reason is hidden. When the direction of magnetization has an in-plane component, the valleys of K and K' points are protected by the mirror symmetry M_{xy}. In other words, when the magnetization direction changes, the valley splitting is influenced by the SOC strength and M_{xy} mirror symmetry.

Besides, to predict the value of valley splitting under the external field, we analyzed the available results. We find that the relationship between valley splitting and onsite correlation, strain, and electric field is linear, while the relationship between valley splitting and the magnetization direction is quadratic. Here, we take strain as an example. The fitting results are shown in Fig. S12 [39]. Their relationship is $y = 2.29x + 21.21$, where x represents the magnitude of strain, and y denotes the valley splitting of the corresponding strain. Thus, you can predict the value of the valley splitting under the external field. $y = a\cos^2 x + b\cos^4 x$ can be used to fit the relationship between the change of magnetization direction and valley splitting.

IV. CONCLUSION

In summary, based on the DFT and effective Hamiltonian model, we predict that antiferromagnetic monolayer MnBr is a ferrovalley material that realizes the anomalous valley Hall effect. The valley splitting of the VBM is 21.55 meV at K and K' points. Importantly, the valley splitting can be effectively regulated by the strain, magnetization rotation, electric field, and built-in electric field. Importantly, the electric field and built-in electric field induce spin splitting due to breaking the P symmetry. Therefore, the spin-layer locked anomalous valley Hall effect can be observed in MnBr. More interestingly, when the ferroelectric substrate Sc_2CO_2 is in the $P\uparrow$ state, the heterostructure shows a metallic property. However, while the electric polarization of Sc_2CO_2 switches to the $P\downarrow$ state, the heterostructure becomes a valley polarization semiconductor. Our work not only enriches the valley physics, but also provides a variety of ways to tune valley splitting.

ACKNOWLEDGMENTS

This work is supported by the National Natural Science Foundation of China (Grants No. 12474238 and No. 12004295), the Natural Science Foundation of Guizhou Provincial Education Department of China (Grant No. ZK[2022]558), P.L. also acknowledge support from the China's Postdoctoral Science Foundation funded project (Grant No. 2022M722547), the Fundamental Research Funds for the Central Universities (xxj03202205), the Open Project of State Key Laboratory of Surface Physics (No. KF2024_02), and the Open Project of State Key Laboratory of Silicon and Advanced Semiconductor Materials (No. SKL2024-10). Y.S. acknowledge support from the NSF of Tongren Science and Technology Bureau (Grant No. [2023]41).

---

[1] D. Xiao, W. Yao, and Q. Niu, Valley-contrasting physics in graphene: Magnetic moment and topological transport, Phys. Rev. Lett. **99**, 236809 (2007).

[2] T. Cao, G. Wang, W. Han, H. Ye, C. Zhu, J. Shi, Q. Niu, P. Tan, E. Wang, B. Liu, and J. Feng, Valley-selective circular dichroism of monolayer molybdenum disulphide, Nat. Commun. **3**, 887 (2012).

[3] K. F. Mak, K. He, J. Shan, and T. F. Heinz, Control of valley polarization in monolayer MoS_2 by optical helicity, Nat. Nanotechnol. **7**, 494 (2012).

[4] H. Zeng, J. Dai, W. Yao, D. Xiao, and X. Cui, Valley polarization in MoS_2 monolayers by optical pumping, Nat. Nanotechnol. **7**, 490 (2012).

[5] M. Wang, S. Cai, C. Pan, C. Wang, X. Lian, Y. Zhuo, K. Xu, T. Cao, X. Pan, B. Wang, S. J. Liang, J. J. Yang, P. Wang, and F. Miao, Robust memristors based on layered two-dimensional materials, Nat. Electron. **1**, 130 (2018).

[6] X. Liu, and M. C. Hersam, 2D materials for quantum information science, Nat. Rev. Mater. **4**, 669 (2019).

[7] P. Li, X. S. Zhou, and Z. X. Guo, Intriguing magnetoelectric effect in two-dimensional ferromagnetic/perovskite oxide ferroelectric heterostructure, npj Comput. Mater. **8**, 20 (2022).

[8] P. Li, J. Z. Zhang, Z. X. Guo, T. Min, and X. R. Wang, Intrinsic anomalous spin Hall effect, Sci. China Phys. Mech. **66**, 227511 (2023).

[9] J. R. Schaibley, H. Yu, G. Clark, P. Rivera, J. S. Ross, K. L. Seyler, W. Yao, and X. Xu, Valleytronics in 2D materials, Nat. Rev. Mater. **1**, 16055 (2016).

[10] W. Y. Tong, S. J. Gong, X. Wan, and C. G. Duan, Concepts of ferrovalley material and anomalous valley Hall effect, Nat. Commun. **7**, 13612 (2016).

[11] H. Hu, W. Y. Tong, Y. H. Shen, X. Wan, C. G. Duan, Concepts of the half-valley-metal and quantum anomalous valley Hall effect, npj Comput. Mater. **6**, 129 (2020).

[12] R. Peng, Y. Ma, X. Xu, Z. He, B. Huang, and Y. Dai, Intrinsic anomalous valley Hall effect in single-layer Nb_3I_8, Phys. Rev. B **102**, 035412 (2020).

[13] K. Wang, Y. Li, H. Mei, P. Li, and Z. X. Guo, Quantum anomalous Hall and valley quantum anomalous Hall effects in two-dimensional d^0 orbital XY monolayers, Phys. Rev. Mater. **6**, 044202 (2022).

[14] P. Li, C. Wu, C. Peng, M. Yang, and W. Xun, Multifield tunable valley splitting in two-dimensional MXene Cr_2COOH, Phys. Rev. B **108**, 195424 (2023).

[15] P. Li, X. Yang, Q. S. Jiang, Y. Z. Wu, and W. Xun, Built-in electric field and strain tunable valley-related multiple topological phase transitions in $VSiXN_4(X = C, Si, Ge, Sn, Pb)$ monolayers. Phys. Rev. Mater. **7**, 064002 (2023).

[16] P. Li, B. Liu, S. Chen, W. X. Zhang, and Z. X. Guo, Progress on two-dimensional ferovalley materials, Chin. Phys. B **33**, 017505 (2024).

[17] Y. Wu, J. Tong, L. Deng, F. Luo, F. Tian, G. Qin, and X. Zhang, Coexisting ferroelectric and ferrovalley polarizations in bilayer stacked magnetic semiconductors, Nano Lett. **23**, 6226 (2023).

[18] W. Xun, C. Wu, H. Sun, W. Zhang, Y. Z. Wu, and P. Li, Coexisting magnetism, ferroelectric, and ferrovalley multiferroic in stacking-dependent two-dimensional materials, Nano Lett. **24**, 3541 (2024).

[19] S. D. Guo, L. Zhang, Y. Zhang, P. Li, and G. Wang, Large spontaneous valley polarization and anomalous valley Hall effect in antiferromagnetic monolayer Fe_2CF_2, Phys. Rev. B **110**, 024416 (2024).

[20] A. M. Jones, H. Yu, J. S. Ross, P. Klement, N. J. Ghimire, J. Yan, D. G. Mandrus, W. Yao, and X. Xu, Spin-layer locking effects in optical orientation of exciton spin in bilayer WSe_2 Nat. Phys. **10**, 130 (2014).

[21] L. Li, L. Shao, X. Liu, A. Gao, H. Wang, B. Zheng, G. Hou, K. Shehzad, L. Yu, F. Miao, Y. Shi, Y. Xu, and X. Wang, Room-temperature valleytronic transistor, Nat. Nanotechnol. **15**, 743 (2020).

[22] A. Zhang, Z. Gong, Z. Zhu, A. Pan, and M. Chen, Effects of the substrate-surface reconstruction and orientation on the spin valley polarization in $MoTe_2$/EuO, Phys. Rev. B **102**, 155413 (2020).

[23] Z. He, R. Peng, X. Feng, X. Xu, Y. Dai, B. Huang, and Y. Ma, Two-dimensional valleytronic semiconductor with spontaneous spin and valley polarization in single-layer Cr_2Se_3, Phys. Rev. B **104**, 075105 (2021).

[24] X. W. Shen, W. Y. Tong, S. J. Gong, and C. G. Duan, Electrically tunable polarizer based on 2D orthorhombic ferrovalley materials, 2D Mater. **5**, 011001 (2017).

[25] Y. Lai, Z. Song, Y. Wan, M. Xue, C. Wang, Y. Ye, L. Dai, Z. Zhang, W. Yang, H. Du, and J. Yang, Two-dimensional ferromagnetism and driven ferroelectricity in van der Waals $CuCrP_2S_6$, Nanoscale **11**, 5163 (2019).

[26] T. Jungwirth, J. Sinova, A. Manchon, X. Marti, J. Wunderlich, and C. Felser, The multiple directions of antiferromagnetic spintronics, Nat. Phys. **14**, 200 (2018).

[27] P. Li, X. Li, J. Feng, J. Ni, Z. X. Guo, and H. Xiang, Origin of zigzag antiferromagnetic order in $XPS_3(X = Fe, Ni)$ monolayers, Phys. Rev. B **109**, 214418 (2024).

[28] P. E. Blöchl, Projector augmented-wave method, Phys. Rev. B **50**, 17953 (1994).

[29] G. Kresse, and J. Furthmuller, Efficient iterative schemes for ab initio total-energy calculations using a plane-wave basis set, Phys. Rev. B **54**, 11169 (1996).

[30] J. P. Perdew, K. Burke, and M. Ernzerhof, Generalized gradient approximation made simple, Phys. Rev. Lett. **77**, 3865 (1996).

[31] P. Li, and T. Y. Cai, Two-dimensional transition-metal oxides Mn_2O_3 realized the quantum anomalous Hall effect, J. Phys. Chem. C **124**, 12705 (2020).

[32] P. Li, and Z. X. Guo, The Dirac half-semimetal and quantum anomalous Hall effect in two-dimensional Janus $Mn_2X_3Y_3$ (X, Y = F, Cl, Br, I), Phys. Chem. Chem. Phys. **23**, 19673 (2021).

[33] H. Sun, Y. Ren, C. Wu, P. Dong, W. Zhang, Y. Wu, and P. Li, Ferroelectric tuning of the valley polarized metal-semiconductor transition in $Mn_2P_2S_3Se_3/Sc_2CO_2$ van der Waals heterostructures and application to nonlinear Hall effect devices, arXiv:2409.06181.

[34] S. Grimme, J. Antony, S. Ehrlich, and H. Krieg, A consistent and accurate *ab initio* parameterization of density functional dispersion correction (DFT-D) for the 94 elemenets H-Pu, J. Chem. Phys. **132**, 154104 (2010).

[35] A. Togo, and I. Tanaka, First principles phonon calculations in materials science, Scr. Mater. **108**, 1 (2015).

[36] S. Nose, A unified formulation of the constant temperature molecular dynamics methods, J. Chem. Phys. **81**, 511 (1984).

[37] A. A. Mostofi, J. R. Yates, Y. S. Lee, I. Souza, D. Vanderbilt, and N. Marzari, wannier90: A tool for obtaining maximally-localised Wannier functions, Comput. Phys. Commun. **178**, 685 (2008).

[38] A. A. Mostofi, J. R. Yates, G. Pizzi, Y. S. Lee, I. Souza, D. Vanderbilt, and N. Marizari, An updated version of wannier90: A tool for obtaining maximally-localised Wannier functions, Comput. Phys. Commun. **185**, 2309 (2014).

[39] See Supplemental Material at http://link.aps.org/supplemental/10.1103/PhysRevB.111.085432 for the band structures of monolayer MnBr with the HSE06 method, the projected density of states for monolayer MnBr, the band structures of monolayer MnBr for the different Hubbard U, the band structures of monolayer MnBr under various strain, the spin splitting under an external electric field, the band structures of monolayer Mn_2BrI, the plane averaged electrostatic potential of monolayer Mn_2ClBr and Mn_2BrI, the structures and band structures of $MnBr/Sc_2CO_2$ for top-Sc and top-O configurations, the variation of SOC strength of Mn atoms in MnBr under an external field, the fitted functional relationship between strain and valley splitting, the total energies of $MnBr/Sc_2CO_2$ heterostructure, and the MAE of $MnBr/Sc_2CO_2$ heterostructure.

[40] P. Li, X. Li, W. Zhao, H. Chen, M. X. Chen, Z. X. Guo, J. Feng, X. G. Gong, and A. H. MacDonald, Topological Dirac states beyond π-orbitals for silicene on SiC(0001) surface, Nano Lett. **17**, 6195 (2017).

[41] T. Liu, D. Xiang, H. K. Ng, Z. Han, K. Hippalgaokar, A. Suwardi, J. Martin, S. Garaj, and J. Wu, Modulation of spin

dynamics in 2D transition-metal dichalcogenide via strain-driven symmetry breaking, Adv. Sci. **9**, 2200816 (2022).

[42] Q. Lu, P. Li, Z. Guo, G. Dong, B. Peng, X. Zha, T. Min, Z. Zhou, and M. Liu, Giant tunable spin Hall angle in sputtered $\mathrm{Bi_2Se_3}$ controlled by an electric field, Nat. Commun. **13**, 1650 (2022).

[43] X. Y. Dong, J. F. Wang, R. X. Zhang, W. H. Duan, B. F. Zhu, J. O. Sofo, and C. X. Liu, Electrically tunable multiple Dirac cones, in thin films of the $\mathrm{(LaO)_2(SbSe_2)_2}$ family of matrials, Nat. Commun. **6**, 8517 (2015).

[44] A. Y. Lu, H. Zhu, J. Xiao, C. P. Chuu, Y. Han, M. H. Chiu, C. C. Cheng, C. W. Yang, K. H. Wei, Y. Yang, Y. Wang, D. Sokaras, D. Nordlund, P. Yang, D. A. Muller, M. Y. Chou, X. Zhang, and L. J. Li, Janus monolayers of transition metal dichalcogenides, Nat. Nanotechnol. **12**, 744 (2017).